

Quantitative evaluation of noise reduction strategies in dual-energy imaging

Richard J. Warp^{a)}

Department of Biomedical Engineering, Duke University, Durham, North Carolina 27710

James T. Dobbins III^{b)}

Department of Biomedical Engineering, Duke University, Durham, North Carolina 27710, and Department of Radiology, Duke University Medical Center, Durham, North Carolina 27710

(Received 6 March 2002; accepted for publication 15 November 2002; published 17 January 2003)

In this paper we describe a quantitative evaluation of the performance of three dual-energy noise reduction algorithms: Kalender's correlated noise reduction (KCNR), noise clipping (NOC), and edge-predictive adaptive smoothing (EPAS). These algorithms were compared to a simple smoothing filter approach, using the variance and noise power spectrum measurements of the residual noise in dual-energy images acquired with an *a*-Si TFT flat-panel x-ray detector. An estimate of the true noise was made through a new method with subpixel accuracy by subtracting an individual image from an ensemble average image. The results indicate that in the lung regions of the tissue image, all three algorithms reduced the noise by similar percentages at high spatial frequencies (KCNR = 88%, NOC = 88%, EPAS = 84%, NOC/KCNR = 88%) and somewhat less at low spatial frequencies (KCNR = 45%, NOC = 54%, EPAS = 52%, NOC/KCNR = 55%). At low frequencies, the presence of edge artifacts from KCNR made the performance worse, thus NOC or NOC combined with KCNR performed best. At high frequencies, KCNR performed best in the bone image, yet NOC performed best in the tissue image. Noise reduction strategies in dual-energy imaging can be effective and should focus on blending various algorithms depending on anatomical locations. © 2003 American Association of Physicists in Medicine. [DOI: 10.1118/1.1538232]

Key words: dual-energy imaging, noise reduction, flat-panel detector, chest radiography, image processing

I. INTRODUCTION

The recent introduction of flat-panel detectors has renewed interest in advanced applications such as dual-energy imaging. The clinical advantages of dual-energy imaging are the ability to remove structured anatomical noise and improve calcium discrimination.¹⁻⁹ Until recently, the majority of research in dual energy has used computed radiography (CR) systems,^{4,5,8-12} although since the introduction of dual energy in the 1950s¹³ many detectors have been investigated for this application, including computed tomography (CT)^{14,15} and image intensifiers (II).^{16,17} The image quality, as measured by the detective quantum efficiency (DQE), is higher in flat-panel detectors than in computed radiography, and thus flat-panel detectors offer the potential for improved image quality in the tissue and bone images generated by the dual-energy technique.^{18,19} Furthermore, with the higher DQE of flat-panel devices, dose savings in conventional radiographic procedures could be applied to dual-energy imaging, resulting in added diagnostic information without an increase in overall patient exposure.

The improved tissue discrimination possible with dual-energy imaging comes at the cost of increased noise. To combat the concomitant increased stochastic noise and regain the benefits of reducing anatomical noise, noise reduction strategies are often employed in dual-energy imaging.^{7,8,11,20-29} In this paper, we evaluate the performance of several noise reduction techniques by an experimental

method that allows an accurate estimation of the original noise, or "true noise," as well as the estimated and residual noise after noise reduction processing. This experimental methodology allows quantitative optimization of parameters pertinent to each algorithm. After optimization, the performance of each algorithm is compared using quantitative regional measures of pixel variance and noise power spectrum.

II. MATERIALS AND METHODS

A. Dual-energy system

The flat-panel detector used in this study was a prototype *a*-Si TFT detector with a CsI:Tl scintillator from GE Medical Systems (Waukesha, WI). The detector has been thoroughly described and characterized elsewhere.¹⁸ Images of an anthropomorphic phantom were acquired without additional filtration in the beam. The tube kilovoltages for the low- and high-energy images were 60 kV_p and 120 kV_p, respectively. A 13:1 antiscatter grid was also used.

We performed weighted log-subtraction dual-energy reconstruction to generate a tissue-canceled bone image, *B*, and a tissue-replacing-bone tissue image, *T*:

$$\begin{aligned} B &= \ln(I_H) - w_B \cdot \ln(I_L), \\ T &= -\ln(I_H) + w_T \cdot \ln(I_L), \end{aligned} \quad (1)$$

where *I_L* and *I_H* are the pixel intensities in the low- and high-energy images, respectively, and *w_B* and *w_T* are weight-

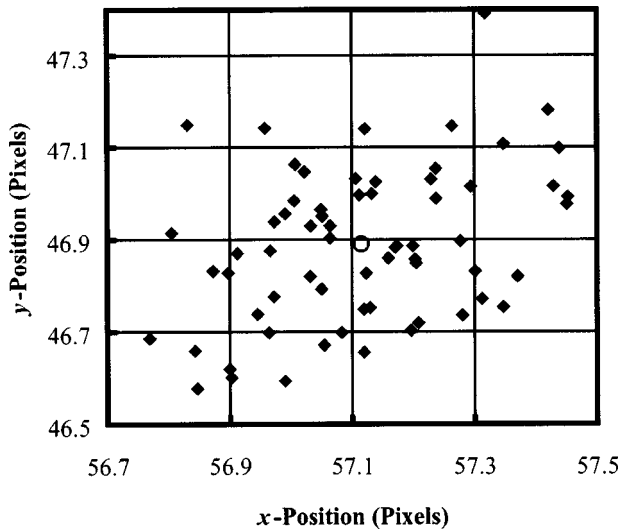


FIG. 1. Projected positions of lead sphere in 66 high-energy images. The average position is marked with a circle (○). Total motion totals less than one pixel with a standard deviation of 0.17 pixels.

ing coefficients to produce the bone and tissue images. The weighting coefficients were manually selected to best eliminate the ribs in the lung area by the choice of w_T , and to best eliminate the pulmonary vasculature in the lung area by the choice of w_B . Log-subtraction weighting coefficients of $w_B = 0.72$ and $w_T = 0.44$ were chosen to meet these criteria, and were held fixed throughout the experiments described.

B. Averaging technique

An estimate of the true anatomical structure was calculated as the ensemble average of 66 images at both 60 and 120 kV_p. The exposure technique was 2.0 and 10 mAs for the high- and low-energy images, respectively. This technique provided a high-energy exposure comparable to a PA chest exam, and a low-energy exposure about one-half that of the PA exam, resulting in a 50% dose increase. The position of the tube, phantom, and detector was held stationary throughout. Raw data were scaled by a multiplicative factor to account for small exposure variations between images. Exposure variations on the order of 0.5%–1.5% were measured by fitting a least-squares zero-intercept linear regression through all pixels in two images. An image “with noise” was taken as a single image; the difference between the single image and the average of 66 images, or “without noise” image, gave an estimate of the “true noise.”

Due to submillimeter vibrations in the prototype system overhead tube support, subpixel misregistration between subsequent images was noticed when using flat-panel subtraction methods. To measure this subpixel misregistration, a small lead sphere was placed on the posterior side of the phantom. The position of the lead sphere was measured by calculating the center of mass of a thresholded, high-pass filtered image. The x and y coordinates of the high-energy image lead sphere positions are plotted in Fig. 1. The range of motion was less than one pixel in either direction with a standard deviation of 0.17 pixels. To correct for the possible

TABLE I. Algorithms for dual-energy noise reduction.

Acronym	Name	References
SSF	Simple smoothing filter	15, 20, 30
KCNR	Kalender's correlated noise reduction	24, 25, 26
NOF	Noise forcing	27, 29
NOC	Noise clipping	27, 29
EPAS	Edge-predictive adaptive smoothing	New

impact of this small misregistration on measurements of image noise, a single image was chosen for analysis such that the lead sphere position was closest radially to the average lead sphere position of the 66 images. Upon image subtraction, the noise estimate showed no visible signs of misregistration using this image. Thus, this image was chosen as the individual image “with noise” to use for all subsequent analyses. However, ensuring that the single image is registered with the average image does not guarantee that the average image is free from misregistration between its constituent images. Consequently, the spatial frequency content of the estimated “true structure” in the average image may differ from the “true structure” in the single image. Again, because the subtraction image noise showed no visible signs of anatomical edges or structures, we inferred that the relative contribution of this misregistration was small compared to the statistical noise itself.

Even after carefully considering subpixel misregistration and subtle exposure variations, the average of $N = 66$ images leaves about $1/\sqrt{N} = 12\%$ residual noise. This residual noise is included in the “true structure” but in reality belongs in the “true noise.” The results presented here should therefore be considered as the ability of noise reduction algorithms to perform on the majority (88%) of the noise in the image.

C. Noise reduction algorithms

The most fundamental noise reduction strategy, both computationally and theoretically, is the application of a simple smoothing filter (SSF). In the early days of dual-energy CT, Rutherford first suggested using a 5×5 boxcar low-pass filter to smooth the noisy reconstructed images.^{15,30} Johns extended the idea to smooth only the high-energy image to avoid blurring calcified structures.²⁰

Driven by the use of dual energy in computed radiography, noise reduction strategies in the late 1980s and 1990s focused on more sophisticated algorithms (Table I). Kalender developed an algorithm called correlated noise reduction (KCNR) that used knowledge about the anticorrelation in noise between the bone and tissue images.²⁴

Kalender²⁴ and Ergun²⁶ proposed methods to improve the performance of KCNR at sharp tissue edges. McCollough²⁵ showed that the algorithm of Kalender²⁴ was analytically related to measurement-dependent filtering methods of Macovski.^{21–23} Kido also proposed an iterative noise reduction method to improve the noise magnitude, edges, and sharpness.^{7,9,31} Several other methods were also introduced,

focusing on improving the sharpness and noise texture, including noise forcing (NOF) and noise clipping (NOC) developed in our laboratory.^{27,29}

Three model-based algorithms are described below and were compared for noise reduction efficacy to a simple smoothing filter (SSF) consisting of a rotationally symmetric Gaussian filter to smooth the high-energy image. The Gaussian function was implemented in Matlab (Mathworks, Natick, MA) with a ROI size of 19 pixels and a FWHM of 4.71 pixels. This filter produces a moderate level of noise reduction while introducing minimal edge artifacts. It served as a simple, though not very sophisticated, baseline against which to compare the three more elaborate noise reduction strategies.

1. Kalender's correlated noise reduction (KCNR)

A regionally optimized nonadaptive form of correlated noise reduction, as described by Kalender,²⁴ McCollough,²⁵ and Ergun,^{26,29} was implemented. Kalender demonstrated that noise in the reconstructed bone and tissue images was anticorrelated.²⁴ They showed how an estimate of the noise in either the bone or tissue image could be used as an estimate of the noise in the complementary image. Using this technique requires knowledge of how the noise is correlated. McCollough²⁵ and Ergun²⁶ independently derived that the noise correlation varies regionally based on the relative noise in the high- and low-energy images. Neither Kalender nor Ergun implemented a regionally optimized algorithm that exploited this varying amount of correlation.

We derived the KCNR-processed bone and tissue images, B^{KCNR} and T^{KCNR} , by adding a weighted version of the anticorrelated noise to the original bone and tissue images, B and T :

$$\begin{aligned} B^{\text{KCNR}} &= B + T_{\text{HPF}}/P_B, \\ T^{\text{KCNR}} &= T + B_{\text{HPF}} \cdot P_T, \end{aligned} \quad (2)$$

where P_B and P_T are weighting coefficients for optimal noise cancellation. The estimated noise was simply a high-pass filtered version of the complementary tissue. The same Gaussian filter mentioned in the previous section was used to implement the high-pass filter for KCNR; the ROI size of 19 pixels and a FWHM of 4.71 pixels were held constant throughout the image. The weighting coefficient used to subtract the estimated noise is discussed below.

The averaging technique we describe in this paper allows an estimate of the true noise in the bone and tissue images. This information allows the KCNR weighting coefficient to be calculated regionally. We chose to optimize the algorithm by minimizing the "true" residual noise variance. Figure 2 shows the optimum weighting parameters for regions of interest in the lung and abdomen areas, as determined by an initial evaluation of the data. The optimal value of the weighting coefficient, P , was about 2.0 for the abdomen in both the bone and tissue images, and between 3–4 for the lung. Figure 2 also corresponds with Fig. 1 of McCollough, where the optimum weighting value, related to the inverse of

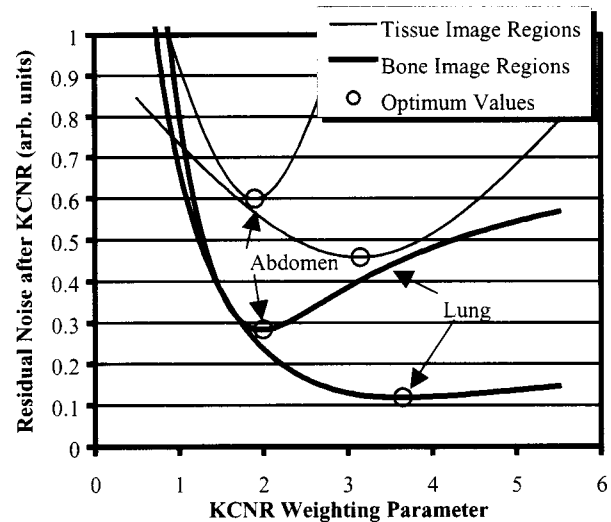


FIG. 2. Optimum KCNR weighting parameters in bone and tissue image regions. Optimal values vary from region to region (e.g., lung and abdomen). Although the two values in the abdomen and two values in the lung are clearly not identical, they are both around 2.0 in the abdomen and around 3–4 in the lung.

the value we derived, was theoretically calculated to be 0.39 for use with an image-intensifier-based dual-energy system.²⁵

Images from the KCNR technique contain artifacts arising from the complementary tissue edge structures. The simple high-pass filtering techniques used to estimate the noise in one image fail to distinguish between random noise and anatomical edges. For example, the noise reduced bone image will contain tissue edges arising from the high-pass filtered version of the tissue image. Kalender proposed three methods to adapt the KCNR algorithm to minimize these edge artifacts.²⁴ Ergun extended the adaptive concept by varying the filter kernel size at suspected edges.²⁶ The edge-adaptive KCNR strategies will only slightly modify the level of aggressiveness of KCNR, while additionally mitigating the edge artifacts. We did not investigate these adaptive strategies.

2. Noise clipping (NOC)

While Kalender's noise reduction method utilizes known mathematical correlations, the noise clipping technique developed at Duke University utilizes known physical relationships between attenuation coefficients in the logarithmically processed high- (H) and low-energy (L) images.²⁷ The anatomical structures present in the L image have greater contrast than the structures in the H image due to greater photoelectric absorption at lower energies. The local contrast of structures was measured by subtracting each pixel value from its local background. The contrast of the H and L values at each (x,y) location pixel was compared, and H pixel values were modified if the contrast exceeded that of the L image (Fig. 3). This algorithm has the advantage of operating on a pixel-by-pixel basis and avoiding the incorporation of neighboring pixels into a blurring process such as with the KCNR technique, thus improving the residual noise texture.

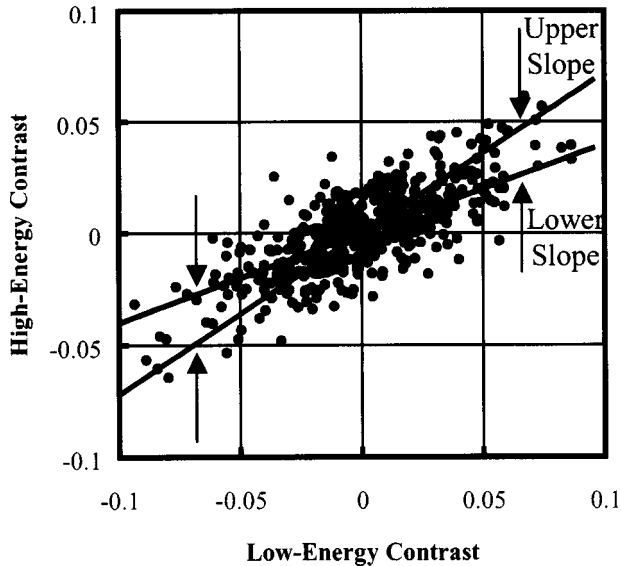


FIG. 3. Noise clipping algorithm. The two lines shown have slopes equal to the dual-energy weighting coefficients for the tissue and bone images. High-energy intensities outside the upper and lower slope lines are clipped either down to the upper line or up to the lower line. Intensities between lines are unchanged.

The NOC implementation used in this paper was nearly identical to that used by Hinshaw.²⁷ A median filter kernel, used to estimate the background signal for computation of pixel-to-pixel contrast, was varied in size over a range of 9–71 pixels. We found visually that large kernels produced greater artifacts at bone edges, while smaller kernels were less effective in estimating low-frequency noise. Based on this visual assessment, a medium-size kernel of 17 × 17 pixels was chosen for this study.

Several methods for modifying the H image pixels were evaluated. Hinshaw reported clipping the H pixels down to a level that would match the contrast of the L image.²⁷ By relating the NOC estimated noise to the true noise, we found that a better method is to clip the H pixels to the expected contrast ratio between the H and L image as actually measured in a given image pair. From theoretical considerations, the contrast ratio should not exceed the log-subtraction weighting value if a pixel contained only tissue ($w_B=0.72$) and should not be less than the log-subtraction weighting value if a pixel contained only bone in a neighborhood of an equal amount of tissue ($w_T=0.44$). Therefore, the most aggressive constraint was for H pixels to be either clipped down to a value making a contrast ratio with the L image of 0.72 or up to make a contrast ratio of 0.44 (Fig. 3). All pixels having a contrast ratio between 0.44 and 0.72 were left unchanged. For the sake of comparison, this lower contrast ratio was varied from a value of 0.44 to lower values and eventually to zero with a reduction in noise suppression but with also fewer artifacts as the value was reduced. A value of zero is what Hinshaw reported and leads to the least aggressive noise reduction.²⁷ To closely match the performance of KCNR for an initial evaluation of NOC, we elected to clip H

pixel values down to a value of 0.72 and up to a value of 0.44.

In addition to performing NOC and KCNR individually, KCNR was also performed on the NOC processed bone and tissue images (indicated as NOC⇒KCNR) using the same regionally optimized set of KCNR parameters.²⁷ The high-energy pixel values were clipped up to a lower level of only 0.2 when used in combination with KCNR, in contrast to being clipped up to w_T when NOC was performed alone. In effect, the NOC algorithm reduced the noise in the high-energy image, and KCNR then reduced any residual, anticorrelated noise in the bone and tissue images.

3. Edge-predictive adaptive smoothing (EPAS)

The third noise reduction technique evaluated was a new method that extends the idea of Johns to smooth the high-energy image,²⁰ by incorporating an adaptive template constraint. The goal of smoothing the high-energy image is to preserve the bone structures. The low-energy image can serve to first locate the bone edges. Based on the location of the bone edges, the amount of smoothing can be varied, because the low-energy image has bone edges with a contrast several times greater than the amplitude of the noise, especially in the lung regions. The filtering of the high-energy image can be made adaptive by simply multiplying the filter kernel element-by-element times a weighting function that depends on the low-energy image. One of the three adaptive methods proposed by Kalendar, termed the “directional filter,” uses an identical concept to modify the filtering kernel for KCNR.²⁴

Mathematically, a simple low-pass filter, LPF, applied to the high-energy image, H , can be made adaptive by multiplying each pixel in the filter kernel by a weighting, $W(L)$, based on low-energy image content:

$$H^{\text{EPAS}} = H \otimes [\text{LPF} \cdot W(L)]$$

$$[\] \Rightarrow \text{normalization} \quad \sum_{m,n} W(L) = 1, \quad (3)$$

where the product (\cdot) between LPF and W is an element by element multiplication. The weighting kernel is normalized so that the sum equals unity. For a weighting kernel centered at pixel (i,j) , the difference between pixel (m,n) and pixel (i,j) in the low-energy image determines the “signal,” whereas the noise in pixel (i,j) determines the “noise:”

$$W_{m,n}(L) = \begin{cases} 1 - \frac{|L_{m,n} - L_{i,j}|}{\beta \cdot \sigma(L_{i,j})}, & |L_{m,n} - L_{i,j}| < \beta \cdot \sigma(L_{i,j}), \\ 0, & \text{otherwise.} \end{cases} \quad (4)$$

Large signals, $|L_{m,n} - L_{i,j}|$, relative to the noise, $\sigma(L_{i,j})$, are indicative of bone and cause the weight values to approach zero, thus excluding likely bone pixels from the smoothing kernel. The overall strength of the algorithm is controlled by

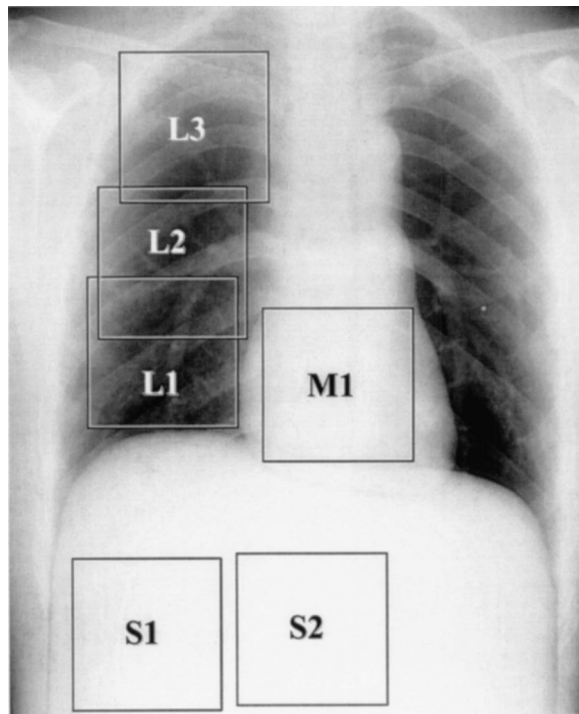


FIG. 4. Locations of ROIs for noise reduction evaluation. Three lung regions, one mediastinum region, and two subdiaphragm regions were used.

the parameter, β , that controls the expected ratio of signal to noise. A value of $\beta=1.5$ was subjectively chosen as the best noise reduction.

D. Variance analysis

The residual noise with each noise reduction technique was measured in six regions of interest (ROI) from the bone and tissue images (Fig. 4). The noise in each ROI was measured as the standard deviation of the residual noise distribution. The residual noise was estimated by subtracting a single image from the ensemble average of 66 images.

E. Power spectral analysis

The residual noise with each technique was also analyzed by measuring the regional two-dimensional noise power spectrum (2D-NPS), a well-established method to evaluate the spatial frequency characteristics and texture of a noise signal.^{32–35} The regional NPS was used to evaluate noise characteristics in the lung, mediastinum, and subdiaphragm. Regions of interest (ROI) containing 384^2 pixels (7.68 cm^2) were chosen to compute the 2D-NPS using the periodogram technique of Welch.³⁵ The ensemble average was computed over subregions of size 64^2 pixels (1.28 cm^2). No zero padding, overlapping, or windowing was used to avoid blurring of sharp power spectral spikes, such as from the presence of the antiscatter grid. The statistical differencing methods of Giger,³² Granfors,¹⁹ and Dobbins³⁶ were used with $N=66$ images, a factor of $N/(N-1)$ accounts for residual noise power after averaging 66 images. Finally, the radial average NPS was computed from the 2D-NPS to reduce the data to one dimension for easy comparison.¹⁹ The data exhibited minimal elevated trends on-axis, such as those present in CR flat-field images.^{34,37} The NPS were nearly radially symmetric, but not exactly so. Hence, the radial 1D-NPS was used as an estimate of the shape of the full 2D-NPS.

The data used to compute the NPS must contain sufficient bit depth to avoid errors from bit quantization. The least number of bits in the noise signal before log transformation was approximately 4.7 in the abdomen of the low-energy image. This bit quantization produces no more than 1%–2% error in the NPS according to an analysis that is similar to that of Giger.³²

III. RESULTS

A. Variance comparison

Characteristic measurements of the standard deviation of pixel values following noise reduction in the lung, retrocardiac mediastinal, and subdiaphragmatic regions are tabulated in Table II. The values listed represent the percentage of the

TABLE II. Percentage of noise (standard deviation) reduced in ROIs shown in Fig. 4. Note: L=lung, M=mediastinum, S=subdiaphragm.

Algorithm	Bone image					
	L1	L2	L3	M1	S1	S2
SSF on H	-11.2	-1.0	3.85	8.5	14.9	8.5
KCNR	51.6	55.6	59.5	67.3	64.1	67.7
NOC	51.9	55.0	56.0	60.0	63.7	60.6
EPAS	49.6	48.9	43.3	16.9	16.2	11.9
NOC⇒KCNR	46.4	52.3	58.8	69.6	65.4	70.1
Algorithm	Tissue image					
	L1	L2	L3	M1	S1	S2
SSF on H	-16.8	-1.9	5.7	19.0	29.2	19.0
KCNR	55.7	56.0	54.1	64.0	63.0	64.9
NOC	52.3	56.9	61.1	72.0	75.5	73.0
EPAS	50.1	52.3	53.1	30.9	30.9	23.0
NOC⇒KCNR	57.0	58.8	58.3	68.0	67.7	68.4

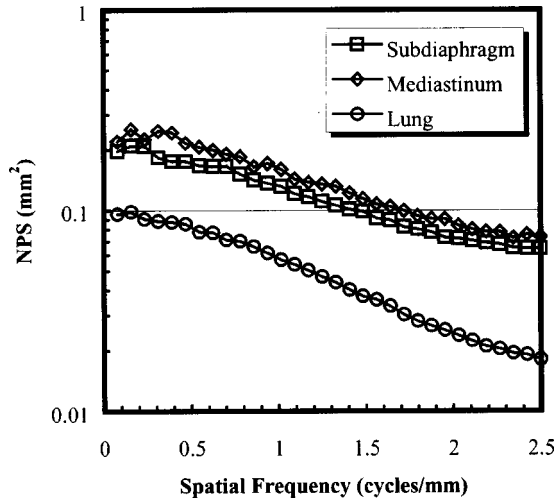


FIG. 5. NPS of three regions in tissue image noise before noise reduction. The subdiaphragm is the average of regions S1 and S2, the lung is the average of regions L1, L2, and L3.

noise removed by the algorithm as measured by the standard deviation before and after processing. Higher values demonstrate improved noise reduction, and negative values represent algorithms that increase the standard deviation in each ROI, often from complementary tissue edge artifacts.

The reduction in noise magnitude was comparable for most algorithms with a few exceptions. The EPAS algorithm performed poorly in the mediastinum and subdiaphragm. Simply smoothing the H image (SSF) actually aggravates the standard deviation measured in the lung regions because of strong bone edge artifacts. The most aggressive algorithm overall was the NOC \Rightarrow KCNR. The NOC portion of the NOC \Rightarrow KCNR combination clipped H pixel values less aggressively than the NOC alone. However, the combination improved the standard deviation performance in some regions.

B. Noise power spectra (NPS) comparison

The noise in the original images varied as a function of the anatomical region in both magnitude and texture. The noise power spectrum (NPS) in the tissue image, without any noise reduction, is plotted for three anatomical regions in Fig. 5. The NPS of the lung was lower than the NPS for the mediastinum or subdiaphragm indicating less noise in the lung in these logarithmically transformed images. The slope of the NPS at high spatial frequencies (1.5–2.5 cycles/mm) was greater in the lung region, indicating a different noise texture. The slightly flatter NPS in the tissue image subdiaphragm ROIs arises from the dominant contribution of the low-energy image, whose NPS at high spatial frequencies is also more flat.

The NPS analysis was used to view the frequency characteristics and noise texture after processing with the noise reduction strategies described previously. Figure 6 shows the 2D-NPS in a subdiaphragm ROI from the bone image after processing with five algorithms. All NPS are displayed on the same intensity scale, lighter intensities indicating lower

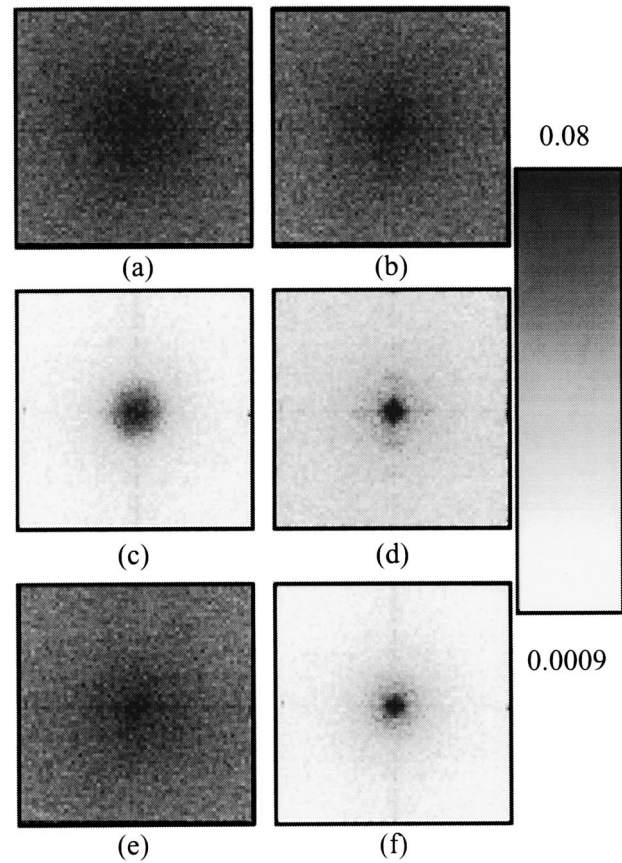


FIG. 6. 2D-NPS on original and residual noise after processing by five algorithms. The subdiaphragm (S2) ROI from the bone image was used. (a) Original noise in bone, (b) SSF, (c) KCNR, (d) NOC, (e) EPAS, and (f) NOC \Rightarrow KCNR. Lighter colored NPS represents lower noise; a log scale is displayed.

noise magnitude. The original 2D-NPS illustrates a high degree of radial symmetry before processing. The SSF and EPAS algorithms did not reduce the noise magnitude much in the subdiaphragm region [Figs. 6(b), 6(e)]. The NOC algorithm reduced the noise more than KCNR at low spatial frequencies, but not at high spatial frequencies [Figs. 6(c), 6(d)]. The NOC \Rightarrow KCNR combined the better low-frequency reduction of NOC with the excellent higher spatial frequency performance of KCNR.

The radial average 1D-NPS computed for all the regions in the bone and tissue images are shown in Fig. 7. The three lung ROIs and the two subdiaphragm ROIs were averaged together. In the mediastinum and subdiaphragm regions, SSF and EPAS performed poorly, as measured by the high NPS values [Figs. 7(b), (c), (e), (f)]. The performance of EPAS was better in the lung regions, whereas low-frequency edge artifacts degrade the SSF performance [Figs. 7(a), 7(d)]. In all regions except the lung in the bone image, combining NOC before KCNR improves the performance of KCNR at low frequencies (below 0.7 cycles/mm).

At higher spatial frequencies, the NPS for NOC performed worse than KCNR in the bone image in all regions. In the tissue image, KCNR performed comparable to NOC at high frequencies in the lung but worse in the mediastinum

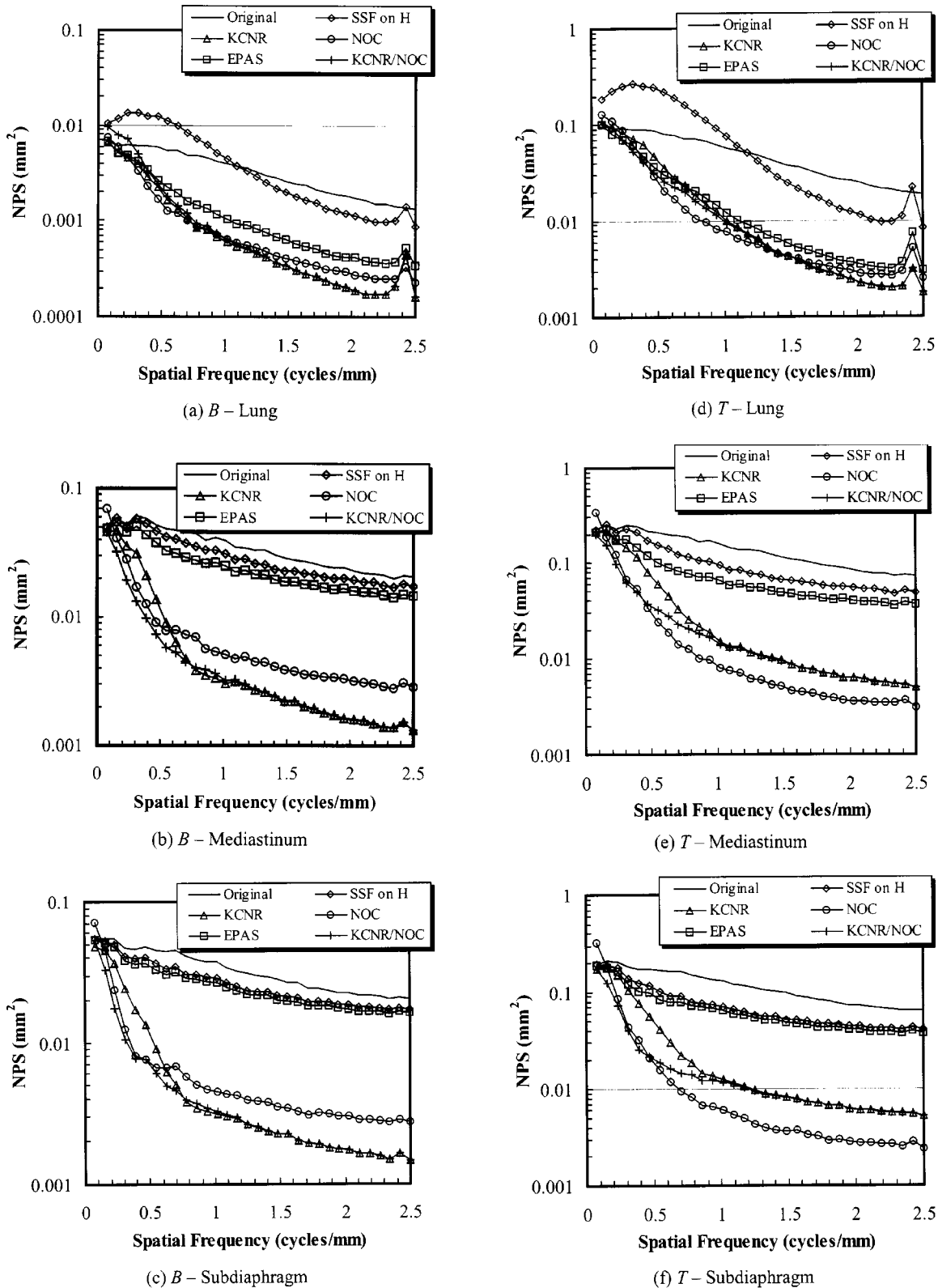


FIG. 7. NPS before and after processing by five algorithms. The average radial NPS over several ROIs was computed in three regions in the bone (B) and tissue (T) images. (a) B—lung, (b) B—mediastinum, (c) B—subdiaphragm, (d) T—lung, (e) T—mediastinum; (f) T—subdiaphragm.

and subdiaphragm. The performances of the individual NOC or KCNR algorithms and the NOC⇒KCNR algorithm were reversed in the bone and tissue images for two reasons. First, the NOC algorithm removes the noise in the high-energy

image, which contributes more to the noise in the tissue image. That causes NOC to reduce the NPS in the tissue image more effectively. Second, NOC alone and NOC⇒KCNR had different clipping values (see Sec. II). This explains why

NOC \Rightarrow KCNR performed worse than NOC alone. The combination performed worse than either individual algorithm in the lung region of the bone image at low-frequencies (less than 0.7 cycles/mm) because of bone artifacts. These artifacts added constructively to enhance the low-frequency noise.

Overall, in the lung region, the NOC, KCNR, and NOC \Rightarrow KCNR techniques performed about equally in both the tissue and bone images, with the KCNR being slightly better at high frequencies. In the dense regions (mediastinum and subdiaphragm) of the bone image, the NOC \Rightarrow KCNR technique worked best overall. In the dense regions of the tissue image, the NOC \Rightarrow KCNR combined technique worked best at low frequencies, and the NOC alone worked best at high frequencies.

IV. DISCUSSION

In this study, images of an anthropomorphic phantom were used for quantitative noise analysis unlike flat-field images used in prior studies.^{25,31} Flat-field images from either slabs of Lucite or bone-equivalent materials provide less informative results when evaluating noise reduction techniques in dual-energy imaging since they fail to account for structured edges, such as those of bones, and variations in noise intensity over anatomical regions. The methods described here fully incorporate spatial variations in spatial-frequency information, anatomical edges, and spatial noise intensity variations into a quantitative method for evaluating noise reduction strategies. It should be noted, however, that the NPS and variance measures reported here cannot differentiate between residual stochastic noise and residual structural artifacts. For example, the bone edges that appear in the tissue image are counted as stochastic noise variance when the KCNR algorithm is evaluated. In addition, the NPS is only theoretically valid for linear shift-invariant systems. The algorithms and experimental system used here are nonlinear and shift-variant, respectively. Thus, NPS measures are only approximations to the actual algorithm performance. Limitations withstanding, the experimental study in this paper demonstrates an effective method for the optimization and evaluation of new image processing algorithms for dual-energy noise reduction.

The potential for global and local physiological motion exists in two-shot dual-energy techniques. Noise reduction algorithms that act individually on the bone or tissue images, such as simple smoothing filters or more advanced structure-based or Wiener adaptive processing, will not depend on any pixel-to-pixel misregistration in the H and L images. However, those algorithms that assume registration between H and L images, such as EPAS and NOC, may be more sensitive to misregistration artifacts. In the middle of these extremes are algorithms like KCNR that use both the B and T images but make no assumptions about anatomical registration. Future considerations must be made for evaluating the effects of misregistration on the noise reduction algorithms.

Clinical implementation and robustness of these algorithms were not tested here. Aside from the expected differ-

ences in how each algorithm will handle misregistration between high- and low-energy images, the algorithms themselves will need to be tested for robustness against varying patient sizes, spatial frequency content, and noise levels. A regionally optimal KCNR algorithm, for example, requires the weighting slope to be modeled as a function of the low-energy image intensity. Similarly, the EPAS algorithm requires models of both how the variance is related to the low-energy image intensity and which β value is best. A third example is the model for computing the bone edges to control the adaptive-KCNR processing. Each of these models that the algorithms require must be tested for clinical robustness over a range of tissue thickness, tissue compositions, scatter magnitudes, and H/L exposure ratios. Furthermore, the use of similar phantom data for the evaluation as well as the optimization of these algorithms means that the results of this work provide only an estimate of the relative performance; future work with a range of clinical images will provide a more refined estimate under clinical conditions.

The exposure techniques used in this paper resulted in low exposures and hence low pixel values in the low-energy abdomen region. This may indicate that electronic noise or system noise was high relative to the quantum statistical noise in that region. Correspondingly, the NPS seen in these dense regions has a less-colored, or more white, spatial-frequency spectrum (Fig. 5). The regions with lower electronic noise and higher signal have less influence from the white electronic noise, and they exhibit a more colored spectrum related more directly to the modulation transfer function (MTF) shape.³³ Another possible explanation for the more whitened noise spectrum in the dense regions is the increase in scatter-to-primary ratio. If the NPS of scattered radiation tends to be white, one may expect the shape may be more white, as we observed. How the NPS shape varies in these fashions should be carefully considered, and possibly incorporated into future noise reduction algorithms.

The noise reduction strategy chosen must not only depend on the algorithm's theoretical performance but also on the actual clinical performance. The clinical performance will include variables such as the ratio of exposures for the high- and low-energy images. This ratio will consequently determine the noise levels present in the images, and the contribution of noise from each image to the bone and tissue images. As the detector and imaging systems evolved from image intensifiers, CT systems, and computed radiography to flat-panel detector systems, the ratio of exposure between high- and low-energy images has changed, impacting the optimal noise reduction strategy. More than the choice of exposure ratios, the system characteristics also have determined the noise levels and contributions between the high- and low-energy images. For example, in single-shot dual-energy imaging with CR, the noise in the high-energy rear screen is higher because the low-energy absorbing front screen attenuates the signal. Consequently, noise reduction strategies in CR require more focus on reducing the noise in the high-energy image, while strategies in flat-panel systems have shifted the focus to the low-energy image. As the flat-panel

systems evolve, the algorithms must be reevaluated and re-optimized.

Future work should include receiver operating characteristic (ROC) observer performance studies to compare the ability of each algorithm to improve nodule detection and/or classification. ROC studies involving either phantom or real patient images could serve as the basis for future clinical evaluations of noise reduction strategies in dual-energy imaging for specific clinical tasks such as nodule detection.

ACKNOWLEDGMENTS

This work was supported in part by grants from the National Institutes of Health (R01 CA55388) and General Electric Medical Systems, and a graduate fellowship from the Whitaker Foundation.

^{a)}Current address: GE Medical Systems, 3000 N. Grandview Blvd., Waukesha, Wisconsin 53188.

^{b)}Electronic mail: jtd@scott.mc.duke.edu

¹L. T. Niklason, N. M. Hickey, D. P. Chakraborty, E. A. Sabbagh, M. V. Yester, R. G. Fraser, and G. T. Barnes, "Simulated pulmonary nodules: Detection with dual-energy digital versus conventional radiography," *Radiology* **160**, 589–593 (1986).

²N. M. Hickey, L. T. Niklason, E. Sabbagh, R. G. Fraser, and G. T. Barnes, "Dual-energy digital radiographic quantification of calcium in simulated pulmonary nodules," *Am. J. Roentgenol.* **148**, 19–24 (1986).

³R. G. Fraser, N. M. Hickey, L. T. Niklason, E. A. Sabbagh, R. F. Luna, C. B. Alexander, C. A. Robinson, A. A. Katzenstein, and G. T. Barnes, "Calcification in pulmonary nodules: Detection with dual-energy digital radiography," *Radiology* **160**, 595–601 (1986).

⁴T. Ishigaki, S. Sakuma, and M. Ikeda, "One-shot dual-energy subtraction chest imaging with computed radiography: Clinical evaluation of film images," *Radiology* **168**, 67–72 (1988).

⁵J. W. Oestmann, R. Greene, J. T. Rhea, H. Rosenthal, R. M. Koenker, C. L. Tillotson, K. D. Pearsen, J. W. Hill, and R. H. Velaj, "Single-exposure dual energy digital radiography in the detection of pulmonary nodules and calcifications," *Invest. Radiol.* **24**, 517–521 (1989).

⁶J. T. Ho and R. A. Kruger, "Comparison of dual-energy and conventional chest radiography for nodule detection," *Invest. Radiol.* **24**, 861–868 (1989).

⁷S. Kido, J. Ikezoe, H. Naito, S. Tamura, T. Kozuka, W. Ito, K. Shimura, and H. Kato, "Single-exposure dual-energy chest images with computed radiography: Evaluation with simulated pulmonary nodules," *Invest. Radiol.* **28**, 482–487 (1993).

⁸F. Kelcz, F. E. Zink, W. W. Pepler, D. G. Kruger, D. L. Ergun, and C. A. Mistretta, "Conventional chest radiography vs dual-energy computed radiography in the detection and characterization of pulmonary nodules," *Am. J. Roentgenol.* **162**, 271–278 (1994).

⁹S. Kido, J. Ikezoe, H. Naito, J. Arisawa, S. Tamura, T. Kozuka, W. Ito, K. Shimura, and H. Kato, "Clinical evaluation of pulmonary nodules with single-exposure dual-energy subtraction chest radiography with an iterative noise-reduction algorithm," *Radiology* **194**, 407–412 (1995).

¹⁰T. Ishigaki, S. Sakuma, Y. Horikawa, M. Ikeda, and H. Yamaguchi, "One-shot dual-energy subtraction imaging," *Radiology* **161**, 271–273 (1986).

¹¹B. K. Stewart and H. K. Huang, "Single-exposure dual-energy computed radiography," *Med. Phys.* **17**, 866–875 (1990).

¹²D. A. Hinshaw and J. T. Dobbins III, "Plate scatter correction for improved performance in dual-energy imaging," *Med. Phys.* **23**, 871–876 (1996).

¹³B. Jacobson, "Dichromatic absorption radiography. Dichromography," *Acta Radiol.* **39**, 437–452 (1953).

¹⁴R. E. Alvarez and A. Macovski, "Energy-selective reconstructions in x-ray computerized tomography," *Phys. Med. Biol.* **21**, 733–744 (1976).

¹⁵R. Rutherford, B. Pullan, and I. Isherwood, "Measurement of effective atomic number and electron density using an EMI scanner," *Neuroradiology* **11**, 15–21 (1976).

¹⁶C. A. Mistretta, M. G. Ort, F. Kelcz, J. R. Cameron, M. P. Siedband, and A. B. Crummy, "Absorption edge fluoroscopy using quasimonochromatic x-ray beams," *Invest. Radiol.* **8**, 402–412 (1973).

¹⁷F. Kelcz and C. A. Mistretta, "Absorption-edge fluoroscopy using a three-spectrum technique," *Med. Phys.* **3**, 159–168 (1976).

¹⁸C. E. Floyd, Jr., R. J. Warp, J. T. Dobbins III, H. G. Chotas, A. H. Baydush, R. Vargas-Voracek, and C. E. Ravin, "Imaging characteristics of an amorphous silicon flat-panel detector for digital chest radiography," *Radiology* **218**, 683–688 (2001).

¹⁹P. R. Granfors and R. Aufrichtig, "Performance of a 41×41-cm² amorphous silicon flat panel x-ray detector for radiographic imaging applications," *Med. Phys.* **27**, 1324–1331 (2000).

²⁰P. C. Johns and M. J. Yaffe, "Theoretical optimization of dual-energy x-ray imaging with application to mammography," *Med. Phys.* **12**, 289–296 (1985).

²¹A. Macovski, D. G. Nishimura, A. Doost-Hoseini, and W. R. Brody, "Measurement-dependent filtering: A novel approach to improved SNR," *IEEE Trans. Med. Imaging* **MI-2**, 122–127 (1983).

²²D. G. Nishimura, A. Macovski, and W. R. Brody, "Noise reduction methods for hybrid subtraction," *Med. Phys.* **11**, 259–265 (1984).

²³Q. Cao, T. Brosnan, A. Macovski, and D. Nishimura, "Least squares approach in measurement-dependent filtering for selective medical images," *IEEE Trans. Med. Imaging* **7**, 154–160 (1988).

²⁴W. A. Kalender, E. Klotz, and L. Kostaridou, "An algorithm for noise suppression in dual energy CT material density images," *IEEE Trans. Med. Imaging* **7**, 218–224 (1988).

²⁵C. H. McCollough, M. S. Van Lysel, W. W. Pepler, and C. A. Mistretta, "A correlated noise reduction algorithm for dual-energy digital subtraction angiography," *Med. Phys.* **16**, 873–880 (1989).

²⁶D. L. Ergun, C. A. Mistretta, D. E. Brown, R. T. Bystranyk, W. K. Sze, F. Kelcz, and D. P. Naidich, "Single-exposure dual-energy computed radiography: Improved detection and processing," *Radiology* **174**, 243–249 (1990).

²⁷D. A. Hinshaw and J. T. Dobbins III, "Recent progress in noise reduction and scatter correction in dual-energy imaging," *Proc. SPIE* **2432**, 134–142 (1995).

²⁸J. T. Dobbins III, "Correlated polarity noise reduction for dual-energy imaging," *Radiology* **201(P)**, 220 (1996).

²⁹D. L. Ergun, W. W. Pepler, J. T. Dobbins III, F. E. Zink, D. G. Kruger, F. Kelcz, F. J. de Bruijn, E. W. Bellers, Y. Wang, R. J. Althof, and M. G. J. Wind, "Dual-energy computed radiography: Improvements in processing," *Proc. SPIE* **2167**, 663–671 (1994).

³⁰R. Rutherford, B. Pullan, and I. Isherwood, "X-ray energies for effective atomic number determination," *Neuroradiology* **11**, 23–28 (1976).

³¹W. Ito, K. Shimura, N. Nakajima, M. Ishida, and H. Kato, "Improvement of detection in computed radiography by new single-exposure dual-energy subtraction," *J. Digit. Imaging* **6**, 42–47 (1993).

³²M. L. Giger, K. Doi, and C. E. Metz, "Investigation of basic imaging properties in digital radiography. 2. Noise Wiener spectrum," *Med. Phys.* **11**, 797–805 (1984).

³³G. T. Barnes, "Radiographic mottle: A comprehensive theory," *Med. Phys.* **9**, 656–667 (1982).

³⁴J. T. Dobbins III, D. L. Ergun, L. Rutz, D. A. Hinshaw, H. Blume, and D. C. Clark, "DQE(f) of four generations of computed radiography acquisition devices," *Med. Phys.* **22**, 1581–1593 (1995).

³⁵A. Oppenheim, R. Schaffer, and J. Buck, *Discrete-Time Signal Processing*, 2nd ed. (Prentice-Hall, Upper Saddle River, 1999).

³⁶J. T. Dobbins III, "Image quality metrics for digital systems," in *Handbook of Medical Imaging—Vol. 1 Physics and Psychophysics*, edited by J. Beutel, H. L. Kundel, and R. L. Van Metter (SPIE, Bellingham, 2000), pp. 161–222.

³⁷M. J. Flynn and E. Samei, "Experimental comparison of noise and resolution for 2k and 4k storage phosphor radiography systems," *Med. Phys.* **28**, 1612–1623 (1999).